

Hot Jupiter engulfment by a red giant in 3D hydrodynamics

Mike Y. M. Lau,^{1,2,3}★ Matteo Cantiello,^{3,4} Adam S. Jermyn,³
Morgan MacLeod,⁵ Ilya Mandel,^{1,2} and Daniel J. Price¹

¹ School of Physics and Astronomy, Monash University, Clayton, Victoria 3800, Australia

² OzGrav: The ARC Centre of Excellence for Gravitational Wave Discovery, Australia

³ Center for Computational Astrophysics, Flatiron Institute, 162 5th Avenue, New York, NY 10010, USA

⁴ Department of Astrophysical Sciences, Princeton University, Princeton, NJ 08544, USA

⁵ Center for Astrophysics | Harvard & Smithsonian, 60 Garden Street, MS-16, Cambridge, MA 02138, USA

Accepted XXX. Received YYY; in original form ZZZ

ABSTRACT

Transit and radial-velocity surveys over the past two decades have uncovered a significant population of short-period exoplanets. Among them are hot Jupiters, which are gas giant planets with orbital periods of a few days and found in 0.1–1 per cent of Sun-like stars. Hot Jupiters are expected to be engulfed during their host star’s radial expansion on the red giant branch. Planetary engulfment has been studied extensively as it may account for observed rapidly rotating and chemically enriched giant stars. We perform 3D hydrodynamical simulations of hot Jupiter engulfment by a 1 M_{\odot} , 4 R_{\odot} early red giant. Our “global” simulations simultaneously resolve the stellar envelope and planetary structure, modelling the hot Jupiter as a polytropic gas sphere. We find that approximately 90 per cent of the hot Jupiter’s mass is ablated in the convective part of the giant envelope, which would enhance the surface lithium abundance by ≈ 0.1 dex. The hot Jupiter is disrupted by a combination of ram pressure and tidal forces near the base of the convective envelope, with the deepest material penetrating to the radiative zone. The star experiences modest spin-up ($\sim 1\text{ km s}^{-1}$), although engulfing a more massive companion could produce a rapidly rotating giant. Drag heating near the surface could exceed the unperturbed stellar luminosity and power an optical transient. For the amount of unbound ejecta recorded in the simulation, H-recombination could also power a transient that is around ten times the pre-engulfment luminosity, for several days.

Key words: planet–star interactions – planets and satellites: gaseous planets – stars: low-mass – hydrodynamics – stars: chemically peculiar – methods: numerical

1 INTRODUCTION

Transit, radial velocity, direct imaging, and microlensing searches have uncovered more than 5,000 confirmed exoplanets over the past two decades, providing valuable insight into their demographics. A substantial fraction of exoplanets are found to have short orbital periods. In particular, hot Jupiters (HJs) are gas giant planets with orbital periods of a few days, and were the first exoplanets discovered around main sequence stars (Mayor & Queloz 1995; Dawson & Johnson 2018; Fortney et al. 2021). Both transit-based (Gould et al. 2006; Bayliss & Sackett 2011; Howard et al. 2012; Fressin et al. 2013) and radial-velocity-based surveys (Marcy et al. 2005; Cumming et al. 2008; Mayor et al. 2011; Wright et al. 2012) find that a few times 0.1 to ≈ 1 per cent of Sun-like stars host HJs.

While the origin of their short orbital periods is interesting by itself, the close proximity of HJs to their host stars also means they should be engulfed by the radial growth of their host

stars, up to an AU on the red giant branch. Star-planet mergers are estimated to occur at a rate of $0.1\text{--}1\text{ yr}^{-1}$ in the Galaxy (Metzger et al. 2012; MacLeod et al. 2018). Processes that shrink a planet’s orbit will cause the planet to become engulfed beneath their present-day separations. Close-in companions ($\lesssim 0.1\text{ AU}$) can be drawn in by tidal dissipation, particularly during post-main-sequence expansion (Rasio et al. 1996; Villaver & Livio 2007, 2009; Jackson et al. 2009; Miller et al. 2009; Kunitomo et al. 2011; Barker 2020; Lazovik 2021). Farther out companions can be brought in via high-eccentricity migration, where the orbit is first driven to be highly eccentric, followed by tidal circularisation at periastron. Mechanisms for increasing the orbital eccentricity include planet-planet scattering (Rasio & Ford 1996; Weidenschilling & Marzari 1996; Jurić & Tremaine 2008; Nagasawa et al. 2008) and (eccentric) Kozai-Lidov oscillations induced by a planetary or stellar companion (Eggleton & Kiseleva-Eggleton 2001; Wu & Murray 2003; Fabrycky & Tremaine 2007; Wu et al. 2007; Naoz et al. 2011, 2012; Stephan et al. 2018).

Planetary engulfment could produce a number of obser-

★ E-mail: mike.lau@monash.edu (MYML)

vational signatures. The engulfed planet's orbital decay may power a luminous transient (Metzger et al. 2012; MacLeod et al. 2018; Yarza et al. 2022; Gurevich et al. 2022). Partial or complete dissolution of the planet in a giant star's convective envelope could chemically enrich the stellar surface (Alexander 1967; Israelian 2002; Aguilera-Gómez et al. 2016; Casey et al. 2019; Soares-Furtado et al. 2021), possibly explaining the existence of some lithium-enriched giant stars (e.g., Monroe et al. 2013; Carlos et al. 2016; Meléndez et al. 2014; Nagar et al. 2019). Observations and canonical stellar models find that surface Li is generally depleted when ascending the red giant branch. This is due to the convective envelope's inward growth during the first dredge-up, which mixes Li-depleted material to the stellar surface. However, $\sim 1\%$ of giant stars are Li rich ($A(\text{Li}) > 1.5^1$), and Li-super-rich ($A(\text{Li}) > 2.7$) giant stars, which have super-meteoritic Li abundances, have also been observed. The angular momentum deposited during planetary engulfment could induce rotational mixing that reaches the H-burning shell, enriching the surface with Li via the Cameron-Fowler process (Cameron & Fowler 1971). The connection between planetary engulfment and these observations is supported by possible correlation of Li enrichment with rotational velocity (Carlberg et al. 2013) and planet occurrence (Adamów et al. 2018).

Understanding the ability for planetary engulfment to produce these effects requires determining the amount of mass lost by the planet in the convective envelope, the dynamical response of the star to the planet's spiral-in, and the distribution of angular momentum following engulfment. These effects are well-suited to be studied with hydrodynamical simulations. However, the large dynamic range spanned by the engulfment process makes it a challenging computational problem, and so various approximations have been made in past simulations. Sandquist et al. (1998, 2002) focused on the local gas flow around engulfed planets, reporting significant dissolution within the stellar envelope. On the other hand, Staff et al. (2016) performed global simulations of a $10 M_J$ planet engulfed by a $3.5 M_\odot$ red giant and by a $3.05 M_\odot$ thermally-pulsating asymptotic giant. They resolve the global envelope structure but approximate the planet as a point mass. Recently, Yarza et al. (2022) simulated the local, steady-state gas flow around an engulfed planet across a parameter space mapped out by analogy with the wind-tunnel formalism developed for studying common-envelope interactions (MacLeod & Ramirez-Ruiz 2015; MacLeod et al. 2017). A key difference is that the perturber is a significant fraction of its Bondi radius, and so is modelled as a rigid sphere with a reflective boundary. Yarza et al. (2022) predict that planetary engulfment could increase the host star's luminosity by several orders of magnitude over $1 - 10^3$ yr, depending on the star's evolutionary stage and the planet mass.

In this study, we combine various aspects of previous approaches, and perform a 3D global hydrodynamical simulation of the engulfment of a $1 M_J$ HJ by a $1 M_\odot$ early-stage red giant. We model the HJ as a gas sphere in order to self-consistently model changes to the planet mass and structure, and the effects of ram-pressure drag or hydrodynamical drag, which is the dominant form of drag for the system at hand (see Section 2.1). Abia et al. (2020) applied a similar approach to modelling the collision between a brown dwarf and a $1 M_\odot$ main-sequence star.

This paper is structured as follows. In Sections 2, we outline

different regimes of star-planet interaction to provide context for our chosen system parameters. In Section 3, we describe the system we simulate and the simulation setup. In Section 4, we present our results, including the different phases of planetary engulfment (Section 4.1), the evolution of the planet velocity (4.2), planet mass ablation (4.3), and the disruption and penetration depth of planetary material (4.4). In Section 5, we discuss possible observational signatures associated with HJ engulfment, including surface chemical enrichment (5.1), induced stellar rotation (5.2), and luminous transients (5.3). We summarise our findings in Section 6.

2 STAR-PLANET INTERACTION REGIMES

The regimes of star-planet interaction may be broadly characterised by the mass ratio, M_p/M_\star , and radius ratio, R_p/R_\star , of the planet and host star. Figure 1 shows the different interaction regimes in $M_p/M_\star - R_p/R_\star$ space. The blue markers indicate engulfment events that would be experienced by confirmed exoplanets in the NASA Exoplanet Archive (Akeson et al. 2013) when their host stars expand to their present-day orbital separations (i.e., taking $R_\star \rightarrow a$). This represents an upper limit to the stellar radius at the moment of engulfment, in the limit of inefficient orbital decay due to tides. The plotted sample comprises 1491 exoplanets with measured R_p , M_p , M_\star , and a . The HJs can be seen to cluster at $M_p/M_\star \sim 10^{-3}$ and $R_p/a \sim 10^{-2}$, whereas the hot Neptunes populate $M_p/M_\star \sim 10^{-5} - 10^{-4}$ and $R_p/a \sim 10^{-3}$.

2.1 Energy dissipation mechanism

An engulfed planet spirals in as orbital energy is dissipated into the stellar envelope by drag forces. The spiral-in time-scale may be estimated as the ratio of the orbital energy to the drag luminosity, $|E_{\text{orb}}|/\dot{E}_{\text{drag}}$. The drag luminosity generally scales as $\dot{E}_{\text{drag}} \sim \rho R_{\text{eff}}^2 v^3$, where ρ is the local density of the background stellar gas, v is the planet velocity relative to this background gas, and R_{eff}^2 is the interaction cross-section with the background medium. This cross-section depends on the dominant form of drag, which can be gravitational drag (Chandrasekhar 1943; Ostriker 1999), or turbulent hydrodynamical/aerodynamic drag. Gravitational drag originates from gravitationally focusing upstream material into a high-density wake that trails the planet. The interaction radius is the planet's Bondi-Hoyle-Lyttleton (BHL) radius (Hoyle & Lyttleton 1939; Bondi 1952), which scales as $R_{\text{eff}} = R_{\text{BHL}} \sim GM_p/v^2$ when the flow is supersonic. On the other hand, hydrodynamical drag arises from the ram pressure of the upstream flow, and so the interaction radius is approximately the planet's geometric radius, $R_{\text{eff}} \approx R_p$.

We can write down the approximate scaling for the dissipation time-scale by taking $\rho \sim M_\star/R_\star^3$ and assuming a Keplerian orbit such that $E_{\text{orb}} \sim -GM_\star M_p/R_\star$ and $v \sim (GM_\star/R_\star)^{1/2}$. Then, the time-scale for energy dissipation by hydrodynamical drag is

$$\frac{|E_{\text{orb}}|}{\dot{E}_{\text{hydro}}} \sim \left(\frac{M_p}{M_\star} \right) \left(\frac{R_p}{R_\star} \right)^{-2} t_{\text{dyn}}, \quad (1)$$

where $t_{\text{dyn}} = [R_\star^3/(GM_\star)]^{1/2}$ is the star's surface free-fall time. Taking instead $R_{\text{eff}} = R_{\text{BHL}} \sim GM_p/v^2$, the timescale for energy dissipation by gravitational drag is

$$\frac{|E_{\text{orb}}|}{\dot{E}_{\text{BHL}}} \sim \left(\frac{M_p}{M_\star} \right)^{-1} t_{\text{dyn}}. \quad (2)$$

¹ The Li relative abundance is defined as $A(\text{Li}) = 12 + \log_{10}[(n(\text{Li})/n(\text{H}))]$, where $n(\text{E})$ is the number of atoms of the element with symbol E.

The boundary between the two regimes is located where $R_p = R_{\text{BHL}}$, i.e., when $R_p/R_\star = M_p/M_\star$, which is plotted as the solid line in Figure 1. Most of the exoplanets, when engulfed by their host stars at their present-day separations, are located in the regime dominated by hydrodynamical drag. Gravitational drag is only relevant for the most massive HJs and for brown dwarfs, or if engulfed by a large, evolved star (Staff et al. 2016). For a regular Jovian planet ($M_p \sim 10^{-3} M_\odot$, $R_p \sim 0.1 R_\odot$), gravitational drag is only important if it is engulfed at $\geq 100 R_\odot$.

In the gravitational drag regime, equation (2) implies that the orbital separation shrinks over many orbits since $M_p \ll M_\star$. This is not necessarily true in the hydrodynamical regime, where equation (1) implies the inspiral can take place over several orbits when $M_p/M_\star \lesssim (R_p/R_\star)^2$. In the more extreme case where $M_p/M_\star \ll (R_p/R_\star)^2$, rather than experiencing a complete inspiral, the drag rapidly dampens the azimuthal orbital velocity and the planet transitions to nearly radial sinking, still mediated by drag.

2.2 Planet Roche-lobe overflow

The shaded region in Figure 1 is unpopulated, as exoplanets in this region would exceed their Roche lobes. A planet that is driven inward into this region via tidal dissipation would therefore avoid direct impact with the stellar envelope (Metzger et al. 2012). Instead, they would either gradually lose their gaseous envelopes in a stable mass transfer episode (Valsecchi et al. 2014, 2015; Jackson et al. 2016; Ginzburg & Sari 2017) or plunge towards the host star due to dynamically unstable mass transfer (Jia & Spruit 2017).

We calculate the boundary of the “Roche-lobe overflow” regime by equating the planet’s Roche limit with its present-day separation ($a_{\text{RLOF}}(M_p/M_\star) = a$), using the Eggleton (1983) approximation to evaluate the Roche radius as a function of mass ratio. For example, a $1 M_J$ and $1 R_J$ planet orbiting a $1 M_\odot$ star has $a_{\text{RLOF}} = 0.01 \text{ AU}$ ($P_{\text{orb}} = 0.4 \text{ d}$). So solar-mass host stars that have evolved beyond the end of the subgiant branch, with radii $R_\star \gtrsim 2 R_\odot$, may directly engulf HJs at their present separations. Engulfment at an earlier evolutionary phase requires the HJ to migrate inward towards the Roche limit (Metzger et al. 2012) or to inflate due to tides and stellar irradiation (e.g., Miller et al. 2009; Komacek et al. 2020).

A number of HJs have been observed to lie near this boundary, as highlighted by some of the square markers in Figure 1. For example, WASP-12b (purple square), a $1.47 M_J$ and $1.9 R_J$ HJ on a 1.09-day orbit (Hebb et al. 2009), is at 80 per cent of its Roche limit. There have been indications that its tenuous, optically-thin exosphere exceeds its Roche lobe and is being gradually transferred onto a debris disk around its host (Li et al. 2010; Fossati et al. 2010).

2.3 Tidal disruption

Planets that enter even smaller radii (inside the shaded region), whether induced by planet-planet scattering or secular chaos (Mardling 1995), or as a result of dynamically unstable mass transfer, could be partially or completely destroyed by tides over multiple periastron encounters, thereby also averting the direct engulfment scenario (Faber et al. 2005; Guillochon et al. 2011; Liu et al. 2013). This occurs near the tidal disruption radius, $r_{\text{td}} = (M_\star/M_p)^{1/3} R_p$. For a $1 M_J$ and $1 R_J$ planet around a $1 M_\odot$ star, $r_{\text{td}} = 1 R_\odot$. Note that r_{td} has the same scaling as the Roche limit, with a prefactor that depends on the planetary structure and the extent of disruption.

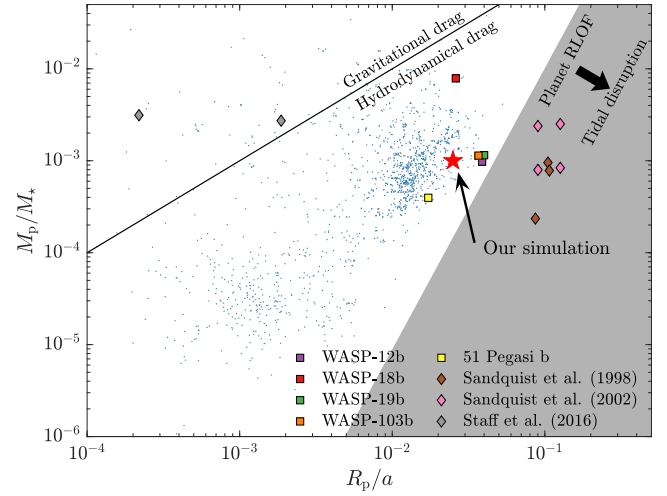


Figure 1. Star-planet interaction regimes in mass and radius ratio space. Blue points correspond to observed exoplanets in the NASA Exoplanet Archive (Akeson et al. 2013), assuming they will be engulfed when their host stars grow to their current separations ($R_\star \rightarrow a$). Square markers highlight specific hot Jupiters while the diamond markers indicate planetary engulfment scenarios explored in past simulations. The solid line is the approximate boundary that determines whether gravitational drag or ram-pressure/hydrodynamical drag dominates in the engulfment process. The shaded area represents an unpopulated region where a planet would exceed its Roche lobe and engage in mass transfer, thus avoiding direct impact with the stellar surface. Planets that are dynamically scattered deep within this region would experience tidal disruption.

Hydrodynamical simulations suggest that disruption could occur out to $2.7 r_{\text{td}}$ (Guillochon et al. 2011).

3 METHODS

3.1 System parameters

Based on the considerations in Section 2, we choose to simulate the engulfment of a $1 M_J$, $1 R_J$ HJ by a $1 M_\odot$ star² that has evolved to a radius of $4 R_\odot$ (0.019 AU), whereupon it is ascending the red giant branch, before the luminosity bump (Figure 2). The red star in Figure 1 shows where our chosen parameters lie in M_p/M_\star – R_p/R_\star space.

The chosen planet mass and radius are typical among the HJ population. However, the 0.019 AU orbital separation (implying $P_{\text{orb}} = 0.9 \text{ d}$) is 2–3 times smaller than the population median (see Figure 1). Nonetheless, this is an interesting and relevant choice for several reasons. Firstly, previous hydrodynamical simulations have either focused on engulfment on notably smaller or larger separations. Staff et al. (2016) used red giant and asymptotic giant branch stars (grey diamond markers in Figure 1), which are qualitatively different to our scenario as gravitational drag drives the spiral-in in their case. Moreover, their large luminosities and deep convective envelopes make it challenging to produce detectable luminous transients and statistically significant chemical enrichment signatures

² More precisely, the simulated HJ has mass of $1.05 M_J$ and radius of $0.97 R_J$. These values are chosen so that the planet-star mass ratio (1.00×10^{-3}) and radius ratio (2.50×10^{-2}) are simple fractions. This difference has little practical importance, and so we simply state the simulated HJ’s initial mass and radius to a single significant figure throughout this paper.

(MacLeod et al. 2018; Soares-Furtado et al. 2021, and also see Section 5). On the other hand, the simulations by Sandquist et al. (1998, 2002) used main-sequence stars, which imply engulfment at even smaller separations. Figure 1 shows that these simulations (brown and pink diamond markers) are located deep within the shaded region. That is, the planet they studied would have experienced intense tidal forces, if not complete disruption, prior to entering the stellar envelope. Thus, we choose simulation parameters that lie safely outside the “Roche-lobe overflow” region.

Our chosen parameters match the handful of so-called ultra-short period HJs that have been observed. For example, WASP-18b (Hellier et al. 2009) and WASP-103b (Southworth et al. 2015), which are labelled in Figure 1, have similar semi-major axes to our simulated system, measuring 0.02026 and 0.01987 AU, respectively. Our simulations could therefore reflect their eventual engulfment if they maintain their present-day separations. Alternatively, a HJ could also be tidally captured from a wider initial orbit and engulfed (Villaver & Livio 2009; Privitera et al. 2016a). WASP-12b is to date the only HJ with a measured orbital decay rate at $29.81 \pm 0.94 \text{ ms yr}^{-1}$, and decay time-scale of $P_{\text{orb}}/\dot{P}_{\text{orb}} = 3.16 \pm 0.10 \text{ Myr}$ (Wong et al. 2022).

3.2 Setup

We performed 3D hydrodynamical simulations of planetary engulfment using the smoothed particle hydrodynamics (SPH; Monaghan 1992; Price 2012) code PHANTOM (v2022.0.1, Price et al. 2018). We resolve the star with $N_{\star} = 10^7$ SPH particles (excluding the H-burning shell and the region interior to it, see Section 3.4) and the planet with 12,300 SPH particles. To check for convergence, we additionally performed a series of simulations at different resolutions ($N_{\star} = 10^6, 3 \times 10^6, 10^7$, and 3×10^7 SPH particles), but with smaller initial separations to balance out the increased computational cost of using higher resolutions than our default.

For all simulations, we use an ideal gas equation of state with an adiabatic index of 5/3. We do not include radiation transport, which is only significant on a time-scale much longer than we simulate (see Section 3.4). We use PHANTOM’s default shock viscosity switch based on Cullen & Dehnen (2010) and default artificial thermal conductivity parameter ($\alpha_u = 1$). To alleviate the computational cost of simulating a large dynamic range, we allow SPH particles to evolve on their individual time-steps, unlike our previous simulations that used global time-stepping (Lau et al. 2022a,b). Our simulation conserves energy to within 1.0 per cent and angular momentum to within 0.9 per cent.

3.3 Hot Jupiter model

We model the HJ as an $n = 3/2$ polytropic gas sphere (Hubbard 1984; Stevenson 1991). Modelling the planet as a gas sphere rather than a point particle (as in Staff et al. 2016) or a rigid sphere (as in Yarza et al. 2022) is relevant for the hydrodynamical drag regime we are exploring and allows us to explore planetary ablation and tidal disruption. Jovian planets are typically thought to have a heavy element core with a supersolar-enriched metallic hydrogen outer layer, and a molecular hydrogen envelope enriched with heavy elements. Our polytropic model neglects this core-envelope structure, but is an adequate approximation since the core contains only a few per cent of the total mass (few tens of M_{\oplus}).

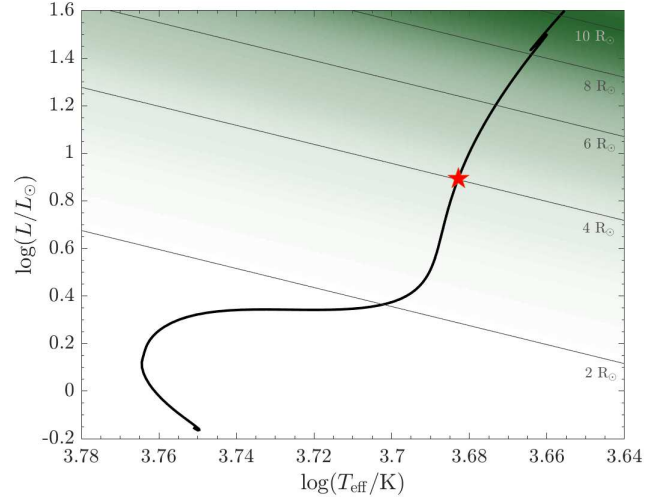


Figure 2. The evolutionary track of our $1 M_{\odot}$ stellar model on the H-R diagram, as calculated by MESA. The red star shows the location of the $4 R_{\odot}$ red giant model used in our simulation. The grey lines are constant radii contours as indicated by their labels. The intensity of green shading is proportional to the density of orbital separations in the NASA Exoplanet Archive.

3.4 Stellar model

To obtain a model for the host star, we used the 1D stellar evolution code MESA (Paxton et al. 2011, 2013, 2015, 2018, 2019) to evolve a $1 M_{\odot}$ star to the red giant phase until reaching $4 R_{\odot}$ in radius³. Figure 2 shows the evolution of our $1 M_{\odot}$ model on the H-R diagram, with the red star marking the selected model. This model has a luminosity of $7.77 L_{\odot}$ and effective temperature of 4,820 K.

Figure 3 shows its density profile (solid line). It consists of a $0.18 M_{\odot}$ inert He core that is $3.3 \times 10^{-2} R_{\odot}$ in size, and a $0.75 M_{\odot}$ and $3.5 R_{\odot}$ deep convective envelope (shaded in grey), separated by a $0.50 R_{\odot}$ radiative zone. The plot is shaded blue according to the specific nuclear burning luminosity, ϵ_{nuc} , showing the location of the H-burning shell. Within the envelope, the convective turnover time ranges from ~ 10 days near the surface to ~ 100 days near the base of the convective zone. This is much longer than the duration we simulate (76 hr) and allows us to neglect the envelope’s convective motion.

The stellar density spans 12 orders of magnitude across the star, which presents a severe dynamic range problem. As with most global hydrodynamical simulations involving giant stars, we replace the dense stellar core, defined as the region beneath some radius r_{core} , with a point mass that interacts via a softened gravitational potential. We use a $0.187 M_{\odot}$ point mass and core radius of $r_{\text{core}} = 0.097 R_{\odot}$ (dotted line in Figure 3), which falls between the H-burning shell and the base of the convective zone. The density profile beneath r_{core} must be replaced with a distribution that is in hydrostatic equilibrium with the softened point mass potential. We solve for this profile, chosen to have constant entropy, according

³ The MESA model and the inlists used to produce it are available at <https://dx.doi.org/10.26180/21342090>. We assume solar metallicity, $Z = 0.0142$, and step overshooting by 0.11 times the pressure scale height (`overshoot_f = 0.11`), using the convective mixing diffusion coefficient at 0.01 times the pressure scale height interior to the step overshoot boundary (`overshoot_f0 = 0.01`).

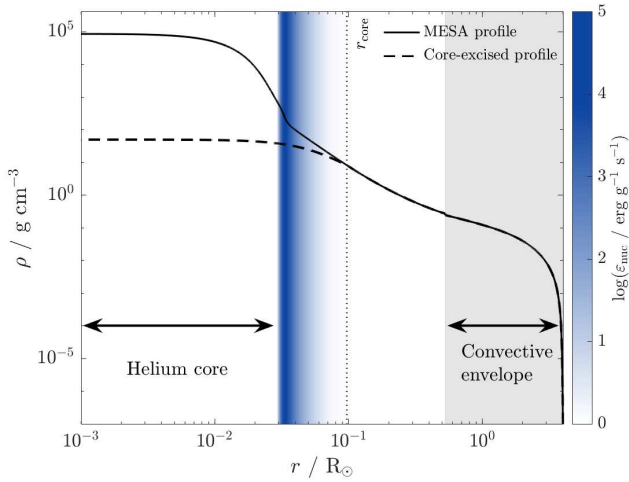


Figure 3. Density profile of the red giant host star as obtained from MESA (solid line) and after excising the high-density “core” (dashed line). The two profiles are identical above $r_{\text{core}} = 0.097 R_{\odot}$ (dotted line). We also show the extent of the convective envelope (grey region) and the He core. The background is shaded blue according to the specific nuclear burning luminosity, ϵ_{nuc} , showing the location of the H-burning shell.

to Section 3.1 of [Gonzalez-Bolivar et al. \(2022\)](#)⁴. The dashed line in Figure 3 shows this modified profile. As can be seen, our point mass replacement lowers the maximum stellar density that has to be resolved by three orders of magnitude.

For both the star and the planet, we use the technique developed in [Lau et al. \(2022a\)](#) (Appendix C) to map a 1D density profile into a 3D distribution of SPH particles that exhibits a high degree of hydrostatic balance and accurately reproduces the intended density profile. We have verified that the host star, when simulated by itself, maintains its radius to within 0.1 per cent and its central density to within 1.2 per cent over the duration of our simulation (or 21 times the surface free-fall time).

3.5 Initial orbit

We assume that the initial star-planet orbit is circular and Keplerian. While many HJs in the 3–10 d period range are observed to have moderate eccentricities ($0.2 < e < 0.6$), consistent with dynamical origins, most with periods $\lesssim 3$ d are consistent with being circular ([Dawson & Johnson 2018](#)), as tidal circularisation becomes very efficient at these small separations ([Dobbs-Dixon et al. 2004](#)). We also assume that both the host star and the HJ are initially non-rotating. The non-rotating assumption is usually made for expanded donors on the giant branch, which are expected to have surface rotational velocities that are a few km s^{-1} (e.g., [Carlborg et al. 2011](#)). On the other hand, short-period hot HJs are expected to have tidally synchronised with their orbits, but the small amount of angular momentum this would contribute ($\lesssim 0.1$ per cent of the orbit) can be safely neglected. The initial separation is chosen such that the star and planet are just touching: $a(t=0) = R_{\star} + R_{\text{p}} = 4.1 R_{\odot}$, with the exception of test simulations in our resolution study (Appendix A), which begin with the planet fully immersed in the stellar envelope, $a(t=0) = 3.8 R_{\odot}$.

⁴ This procedure is automated as a setup option for stars in PHANTOM.

4 RESULTS

4.1 Stages of planetary engulfment

We present our simulation in Figures 4 and 5, which show density slices in the orbital plane at six different points in time. In Figure 5, only SPH particles that initially constituted the HJ (“planet particles”) are rendered. Panel (a) shows the initial setup ($t=0$), while panel (f) shows the end of the simulation.

We identify four different stages of planetary engulfment, similar to the processes described by [Metzger et al. \(2012\)](#) and [Jia & Spruit \(2018\)](#). Figure 6 plots the separation, a , between the stellar core and the planet as a function of time, with these four stages labelled. We define a as the distance between the point-mass stellar core and the currently densest planet particle.

(i) Grazing phase The HJ experiences a relatively long “grazing phase” near the stellar surface (panels (a)–(b)). We label this phase in Figure 6 as the part of the inspiral where the HJ is partially immersed within the stellar envelope ($R_{\star} - R_{\text{p}} < a < R_{\star} + R_{\text{p}}$). This period lasts 35 hr, during which the HJ completes more than one and a half orbits.

As explained in Section 2, hydrodynamical drag drives orbital decay in the simulated regime. In the stellar model, the density scale height near the surface, $H \sim 10^{-2} R_{\odot}$, is a small fraction of the planet radius. H increases with depth, surpassing $R_{\text{p}} = 0.1 R_{\odot}$ upon reaching $a = 3.9 R_{\odot}$, where the HJ becomes fully immersed. Therefore, orbital decay during the grazing phase is driven by interaction with upstream gas that is within a distance H from the planet’s inner edge closest to the stellar centre ([Metzger et al. 2012](#)). The cross-sectional area of this portion of the planet is $\sim R_{\text{p}}^{1/2} H^{3/2}$, and the density of the upstream gas that interacts with this region is approximately $\rho(r = a - R_{\text{p}})$. Therefore, the drag luminosity scales as $\dot{E}_{\text{hydro}} \sim R_{\text{p}}^{1/2} H^{3/2} \rho(r = a - R_{\text{p}}) v^3$.

However, the resolution at the stellar surface limits our ability to accurately resolve the grazing phase. Initially, the surface of the 3D star is resolved down to $10^{-4} \text{ g cm}^{-3}$, which is three orders of magnitude larger than the photospheric density according to the MESA model (see also Appendix A). The minimum resolved density scale height is $\approx 0.3 R_{\odot}$, which is already three times the planet radius. The decay time-scale, set by the time required to migrate inwards by a scale height from the stellar surface, scales as $H^{-1/2} \rho^{-1}$, implying that the drag-dominated part of the grazing phase in our simulations may be $10^3 - 10^4$ times shorter than in actuality. Local simulations (e.g., [Sandquist et al. 1998, 2002](#); [Yarza et al. 2022](#)) or 1D studies (e.g., [Soker et al. 1984](#); [Livio & Soker 1984](#); [Metzger et al. 2017](#)), which may easily resolve the threshold density scale height, are better-suited for studying the grazing interaction.

(ii) Engulfment The main engulfment phase (panels (b)–(d)) follows the grazing phase. The HJ spirals in from $3.9 R_{\odot}$ to $1.0 R_{\odot}$ in 18.5 hr (see Figure 6), approximately completing one orbit. The orbital decay time-scale is therefore comparable with the orbital period ($a/(-\dot{a}) \sim P_{\text{orb}}$). During this phase, the HJ is completely immersed and the local scale height exceeds the planet radius, so that the interaction cross-section is the geometric cross-section, πR_{p}^2 . R_{p}/H ranges from a few times 10^{-1} early on to a few times 10^{-2} deeper within the convective envelope. This means that in the early inspiral, the density gradient of the upstream flow may have a dynamically important effect. This may be modelled as a modification to the drag coefficient, which has been studied extensively in “wind tunnel” simulations (e.g., [MacLeod & Ramirez-Ruiz 2015](#);

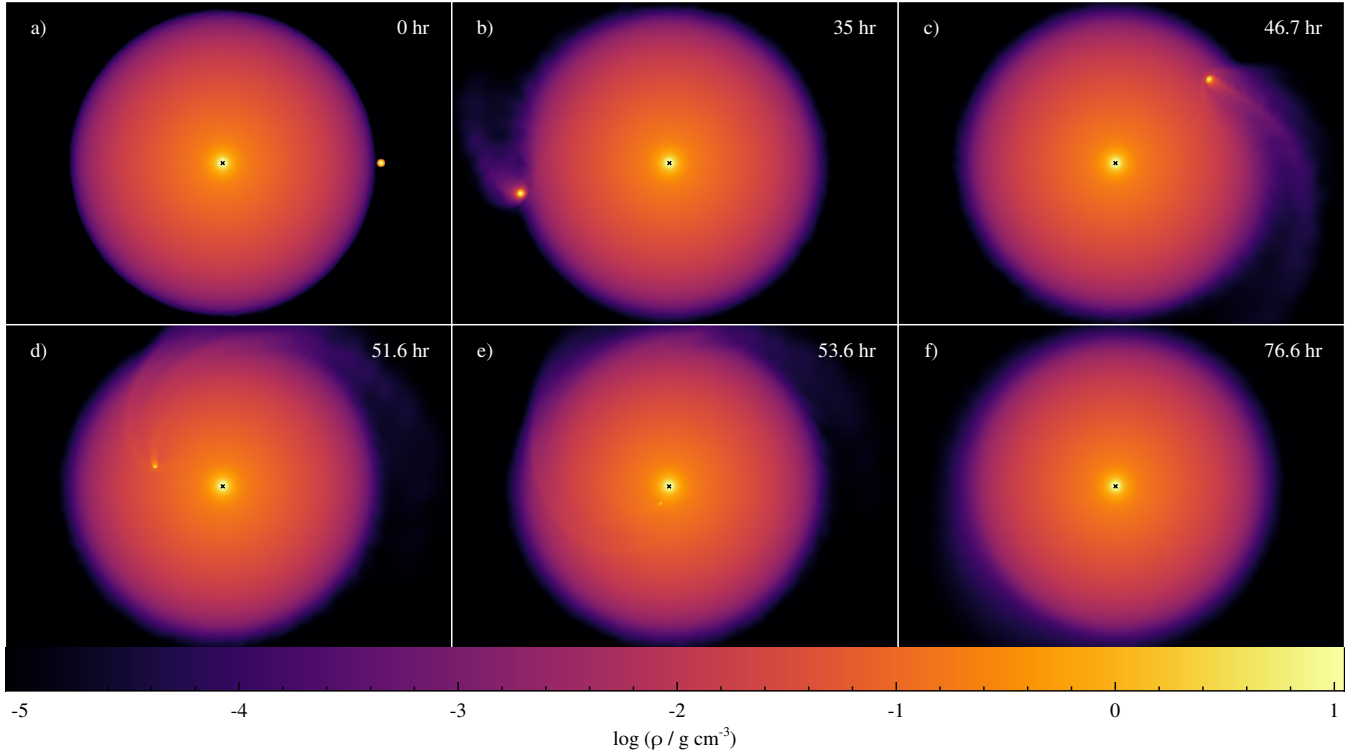


Figure 4. Density slices ($8.4 R_{\odot} \times 11.6 R_{\odot}$) in the orbital plane. (a): Start of the simulation where the hot Jupiter grazes the stellar surface ($P_{\text{orb}} = 23.1$ hr). (b)-(c): The hot Jupiter is fully engulfed and spirals in due to drag. (d)-(e): Radial sinking and disruption of the hot Jupiter. (f): End of simulation. The black cross marks the location of the sink particle used to replace the stellar core. This Figure was created with *SPLASH* (Price 2007). Videos of our simulations are available at https://themikelau.github.io/planet_engulfment.html.

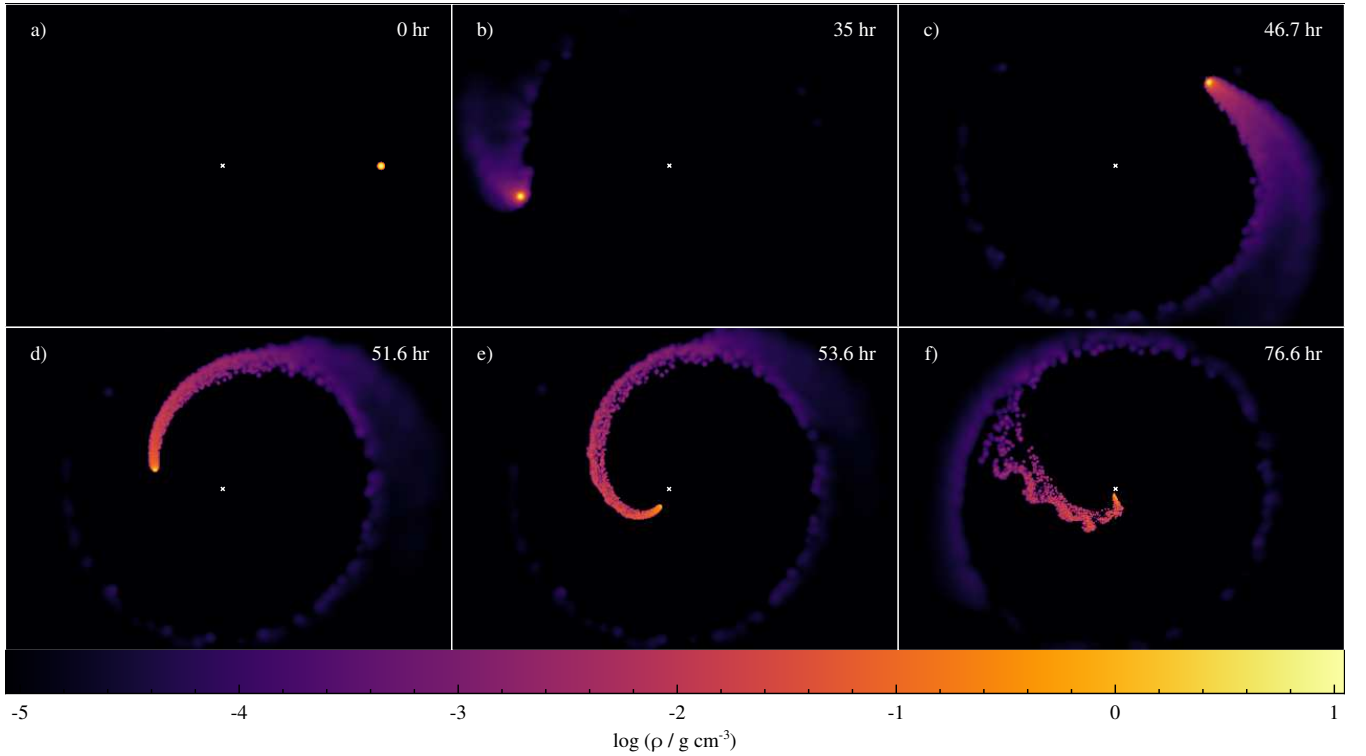


Figure 5. Same as Figure 4, but only showing the planetary material. Note that the observed granularity is an artefact of rendering a restricted number of SPH particles.

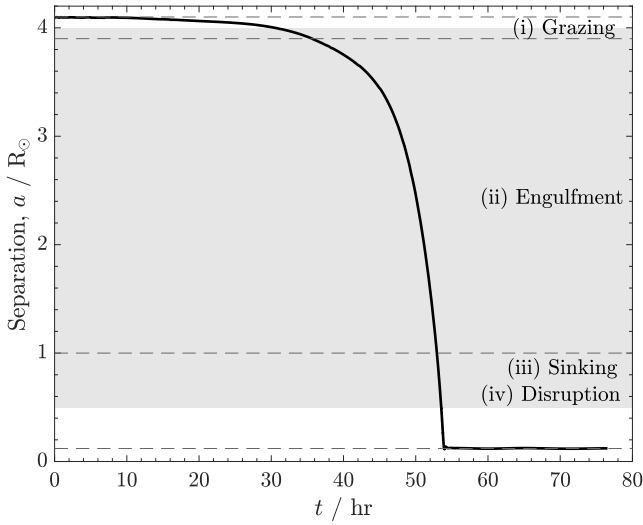


Figure 6. Evolution of the separation, a , between the planet and the stellar core. The horizontal dashed lines mark the boundaries of the grazing and engulfment phases of planetary engulfment that we have identified in Section 4.1. The grey shaded region shows the extent of the convective envelope.

MacLeod et al. 2017; De et al. 2020; Yarza et al. 2022). The HJ’s instantaneous velocity is close to but slightly less than the local Keplerian speed, $v_K = (Gm/a)^{1/2}$ (see Section 4.2), where m is the stellar mass coordinate at the planet’s position. The orbital motion is mildly supersonic relative to the envelope, with $\mathcal{M} \approx 3$, driving a bow shock through the stellar envelope as seen in Figure 4(c)–(e). We also find that the HJ’s mass steadily decreases by ≈ 90 per cent, down to $0.1 M_J$. The ablated material lies in the planet’s wake, as highlighted by Figure 5. The boundary between this material and the stellar gas is susceptible to the Kelvin-Helmholtz instability, which leads to the growth of vortices seen in panel (f). We discuss the HJ’s ablation process in Section 4.3.

(iii) Sinking The sinking phase is characterised by the transition from azimuthal orbital motion to a radial plunge (panels (d)–(e)). In Figure 6, we mark the start of this phase as when the inward radial velocity exceeds the azimuthal velocity, $-v_r > v_\phi$. We reiterate the result from Section 2 that radial descent may only occur in engulfment events driven by hydrodynamical drag, but not gravitational drag, since in the latter regime, the inspiral time-scale is a factor of $M_\star/M_p \gg 1$ longer than the orbital period at contact (following equation (2)). We discuss the transition to sinking in more detail in Section 4.2.

(iv) Disruption The remaining HJ is eventually disrupted near the inner boundary of the convective envelope due to the large stellar densities encountered there, which are conducive to both tidal and ram-pressure disruption. We stop the simulation after the disrupted material approaches rest, at $t = 76.6$ hr (panel (f)), although there is still significant rotational motion near the stellar surface from ablated material and angular momentum deposited during the grazing phase (see Section 5.2). Figure 6 shows that the deepest material settles at $0.1 R_\odot$, penetrating into the radiative region but not beneath the simulation’s inner boundary (i.e. above the H-burning shell). We further discuss the disruption mechanism and the maximum depth reached by the disrupted material in Section 4.4.

4.2 Planet velocity

The top panel of Figure 7 shows components of the HJ’s velocity, \mathbf{v} , as functions of separation. As with the position, we define \mathbf{v} as the velocity of the densest SPH particle that initially makes up the HJ. The planet’s speed, $|\mathbf{v}|$ (red curve), is between $\approx 200 - 240 \text{ km s}^{-1}$ up to the last $\approx 0.2 R_\odot$, upon which the planet is brought to rest. Because $|\mathbf{v}|$ remains mostly constant despite interacting with deeper material with higher sound speeds, the Mach number gradually decreases from ≈ 10 at the start of the engulfment phase to 0.8 upon reaching the sinking phase. This is plotted as the turquoise curve in the bottom panel of Figure 7. The local Keplerian speed, v_K (blue curve), is a reasonable approximation to $|\mathbf{v}|$ until radial motion dominates, after which it is no longer relevant.

The transition to sinking is shown by the increasing radial ($-v_r$, green curve) and diminishing azimuthal (v_ϕ , purple curve) velocity components. At $a = 1 R_\odot$, $-v_r$ exceeds v_ϕ , and for $a \lesssim 0.2 R_\odot$, $|\mathbf{v}|$ is entirely radial and rapidly decreasing in magnitude. Note that the noisiness in these plots at small separations reflects sensitivity to the choice of SPH particle used to define \mathbf{v} .

Neglecting the planet’s inertia during the sinking phase, the radial descent speed is determined by the balance between hydrodynamical drag and gravity (Jia & Spruit 2018):

$$v_{\text{sink}} = \left(\frac{2GmM_p}{\pi R_p^2 \rho a^2} \right)^{1/2} = \left(\frac{2M_p}{\pi \rho R_p^3} \frac{R_p}{a} \right)^{1/2} v_K(a), \quad (3)$$

where we have preserved the factor of π in the HJ’s geometric cross-section and assumed a drag coefficient of $1/2$ appropriate for a smooth sphere at large Reynolds numbers ($Re \gtrsim 10^4$). We have also neglected buoyancy, which is appropriate at least within the convective region, where the mean planet density, $\langle \rho_p \rangle \approx 1.4 \text{ g cm}^{-3}$, is many times greater than the ambient density. We plot v_{sink} as the orange curve in the top panel of Figure 7 for $a < 1.7 R_\odot$. We use the HJ’s instantaneous mass for M_p (see Section 4.3), a fixed radius $R_p = 0.1 R_\odot$, and assume the unperturbed stellar density, $\rho(r = a)$, at the present separation. We find that v_{sink} agrees reasonably with $|\mathbf{v}|$ from $a \lesssim 1.2 R_\odot$, despite the sinking phase only starting at $1.0 R_\odot$. The sharp bump at $a = 0.5 R_\odot$ arises from the density bump at the base of the convective zone. At small separations ($a \lesssim 0.5 R_\odot$), v_{sink} underpredicts the actual speed. This could be because the HJ radius significantly decreases below the assumed $0.1 R_\odot$, and because of rapid mass loss in these dense stellar layers, which could impart a large acceleration onto the planet not accounted for in equation (3).

4.3 Planet ablation

Figure 8 shows the evolution in planet mass, M_p , as a function of the separation, a . We compute M_p by summing the masses of SPH particles that (i) initially made up the HJ, (ii) have velocity projections that are within some threshold of the velocity at the densest point of the HJ, and (iii) are within $2 R_J$ from that densest point. The five different lines in Figure 8, from bottom to top, assume velocity thresholds of $0.1, 0.3, 0.5, 0.7$, and 0.9 (most to least restrictive). We assume a threshold of 0.7 in the rest of the discussion.

The planet loses around 90 per cent of its mass during the engulfment process, consistent with Sandquist et al. (1998), who simulated HJ engulfment by a main-sequence star. Abia et al. (2020) conducted global SPH simulations of brown dwarf engulfment, also finding ablation but concentrated at very large depths. This could be

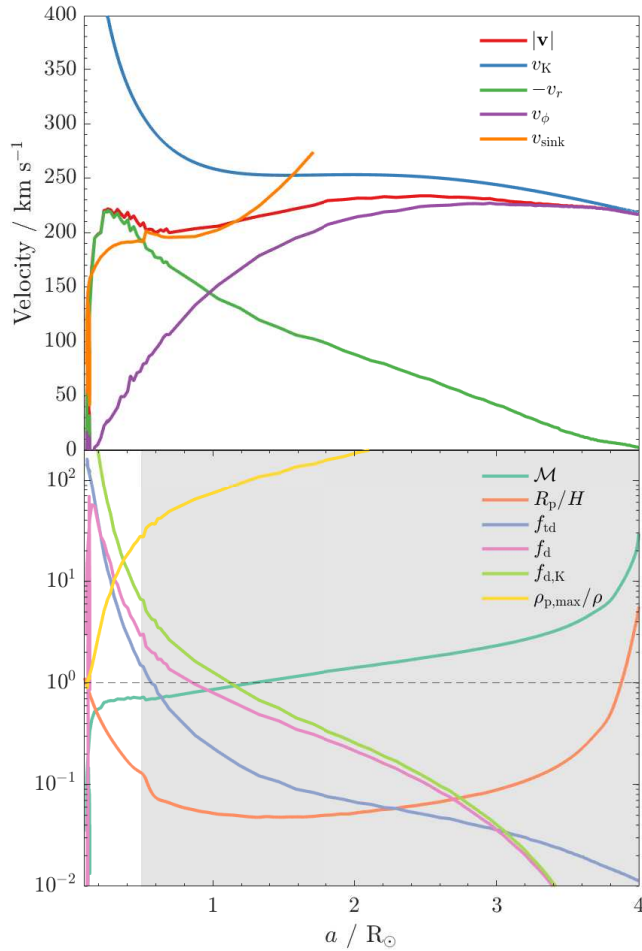


Figure 7. *Top panel:* Evolution of planet velocity components as functions of separation, including the planet speed ($|\mathbf{v}|$), (negative) radial velocity ($-v_r$), and azimuthal velocity (v_ϕ). For comparison, we also show the local Keplerian speed (v_K) and the analytically estimated descent speed (v_{sink}) given by equation (3). *Bottom panel:* Key dimensionless quantities that characterise various processes, including the planet’s Mach number (\mathcal{M}), the ratio of planet radius to density scale height (R_p/H), tidal disruption parameter (f_{id} , equation (7)), ram-pressure disruption parameter (f_{d} , equation (5)), f_{d} evaluated with the Keplerian speed ($f_{\text{d,K}}$), and the ratio of the maximum density inside the planet to the background density ($\rho_{\text{p,max}}/\rho$). The grey region shows the extent of the convective envelope.

because their brown dwarf model is around 10 times more massive than our HJ, and therefore more compact given similar radii.

In Appendix A, we show that the amount of ablated mass at a given time or separation has not fully converged at the current resolution. The initial mass loss, which takes place in low-density surface layers, is overestimated at lower resolutions. This could be because of the larger SPH conductivity used to resolve the contact discontinuity (Chow & Monaghan 1997; Price 2008), which leads to some artificial heating of the HJ. Despite this, the overall amount of ablated mass appears to be relatively robust, i.e., later mass loss occurring in deeper layers adjusts to strip the HJ by a similar overall amount. This could be because the evolution in M_p is roughly determined by pressure equilibrium between the stripped HJ surface and the incident ram pressure. Across all tested resolutions, roughly $0.9 M_J$ of material is deposited into the convective zone, shown as the shaded region in Figure 8. This key quantity determines the

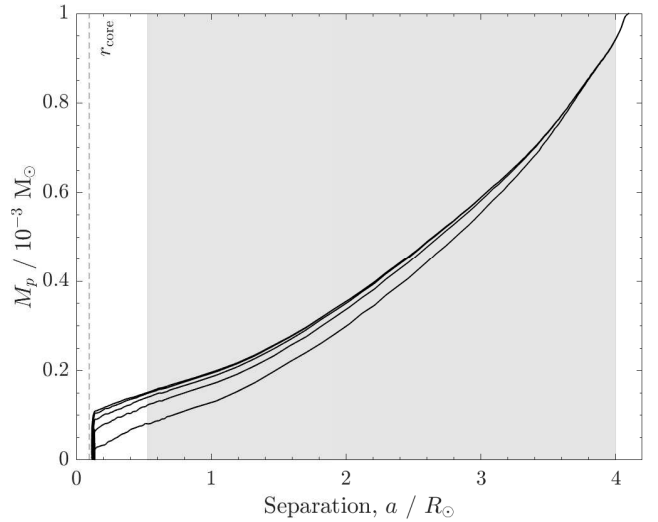


Figure 8. Evolution of the planet mass, M_p , as a function of the separation, a , showing that the hot Jupiter loses around 90 per cent of its mass before disrupting. Around $0.9 M_J$ of material is deposited into the convective zone (grey region). The five different lines estimate M_p according to the different velocity thresholds explained in Section 4.3.

ability for an engulfed HJ to chemically enrich the host’s surface, which we estimate in Section 5.1.

The nearly factor of ten change in planet mass observed in our simulations cautions against assuming M_p to be fixed during planetary engulfment, whether for analytical estimates (e.g., MacLeod et al. 2018; Stephan et al. 2018, 2020; Soares-Furtado et al. 2021) or as a simplifying model assumption (e.g., Staff et al. 2016; Yarza et al. 2022). The gradual mass ablation could be due to shock heating of the HJ, a process that can be studied in detail through local simulations that resolve the planet with high resolution (e.g., Hirai et al. 2014, 2020). That mass loss occurs gradually and not as a single, global episode (Jia & Spruit 2018) could make a significant difference towards the ability for planetary engulfment to enhance the surface chemical abundance of stars (see Sections 4.4 and 5.1).

Mass ablation may also occur via thermal evaporation, where the thermal energy of the background medium overcomes the HJ’s binding energy. This process is not modelled in our simulation, which has no heat transport, and therefore requires separate discussion. Thermal evaporation occurs when the ambient temperature exceeds the HJ’s virial temperature (Livio & Soker 1984; Siess & Livio 1999; Aguilera-Gómez et al. 2016),

$$T_{\text{virial}} \sim \frac{GM_p m_H}{k_B R_p} \approx 2 \times 10^5 \text{ K} \left(\frac{M_p}{M_J} \right) \left(\frac{R_p}{R_J} \right)^{-1}, \quad (4)$$

where m_H is the proton mass and k_B is Boltzmann’s constant. For Jovian planets, T_{virial} greatly exceeds the surface temperature of any host star, meaning thermal evaporation is unimportant during and leading to the grazing phase⁵. Inside a giant star’s convective envelope, the temperature easily exceeds T_{virial} . A key question is therefore whether the duration of the HJ’s dynamical in-fall exceeds the heating time-scale. Giant planets are expected to be largely if not fully convective⁶. Guillot et al. (2004) show that applying

⁵ Although, the shortest-period HJs are known to have inflated radii of up to $2 R_J$, correlated with the level of irradiation (Lopez & Fortney 2016).

⁶ The strong irradiation of HJs, particularly leading up to engulfment, causes

mixing length theory to Jupiter interior models yields convective turnover times of ~ 1 yr in the molecular and metallic regions, which greatly exceed the spiral-in duration. Uncertain effects like rotation, magnetic fields, and compositional gradients are expected to inhibit convection and further lengthen the transport time-scale (Guillot et al. 2004). Thermal evaporation is therefore unlikely to be an important ablation mechanism during engulfment.

4.4 Disruption and penetration depth

The HJ is expected to disrupt at sufficiently large depths. We discuss the expected location and possible mechanisms of disruption. Jia & Spruit (2018) estimate that an engulfed planet dissociates in a global process when the ram pressure overcomes its binding energy. This roughly occurs when the dimensionless disruption parameter, f_d , exceeds unity:

$$f_d \equiv \frac{\rho \Delta v^2}{\langle \rho_p \rangle v_{\text{esc},p}^2} \gtrsim 1, \quad (5)$$

where ρ is the ambient density, Δv is the velocity contrast between the planet and the upstream gas, $\langle \rho_p \rangle = 3M_p/(4\pi R_p^3)$ is the mean planet density, and $v_{\text{esc},p} = (2GM_p/R_p)^{1/2}$ is the planet's escape speed. We have shown that during the grazing and engulfment phases, Δv may be reasonably approximated by the local Keplerian speed, $v_K = (Gm/a)^{1/2}$, in which case the disruption parameter may be written as

$$f_{d,K} = \frac{\rho}{2\langle \rho_p \rangle} \frac{m}{M_p} \frac{R_p}{a}. \quad (6)$$

Tidal forces in the stellar interior may also cause global disruption, which occurs when the volume-averaged stellar density interior to the planet exceeds the mean planet density. That is, the following tidal disruption parameter exceeds unity:

$$f_{td} \equiv \frac{m}{M_p} \left(\frac{R_p}{a} \right)^3 \gtrsim 1. \quad (7)$$

The bottom panel of Figure 7 shows f_{td} , f_d , and $f_{d,K}$ as functions of a . In calculating their values in the simulation, we assume a fixed radius of $R_p = 0.1 R_\odot$ but use the instantaneous mass M_p calculated in Figure 8. We also assume $\rho = \rho(r = a)$ is given by the unperturbed stellar density at the HJ's position. f_d , shown by the pink curve, exceeds unity at $a = 0.83 R_\odot$, within the convective region and near the start of the sinking phase. Because the Keplerian speed overestimates the actual planet speed, and therefore the ram pressure of the incident flow, $f_{d,K}$ reaches unity at a larger radius, $a = 1.1 R_\odot$. On the other hand, f_{td} exceeds unity at $a = 0.57 R_\odot$, which is near but above the convective boundary. The criteria for ram pressure disruption are therefore met before the criterion for tidal disruption. However, because equations (5)–(7) only provide approximate scalings, the locations at which ram-pressure or tidal destruction occur are only known roughly. Also, the scale heights of f_d and f_{td} at the boundaries where they exceed unity, the distance between the two boundaries, and the planet size itself are all comparable. As such, both tides and ram pressure are likely to have played a role in disrupting the HJ near $a \approx 0.6 - 0.8 R_\odot$.

The disrupted planetary material, which is denser than its surroundings, penetrate into deeper layers of the star. Figure 6 shows

that the densest material reaches $\approx 0.1 R_\odot$, which is within the radiative shell. These fragments stall when the density contrast reduces to zero, upon which they become neutrally buoyant (equivalently, they come into entropy equilibrium with their surroundings, e.g., Ivanova et al. 2002). This is illustrated by plotting the ratio $\rho_{p,\text{max}}/\rho$ of the maximum planet density to the ambient density, shown as the yellow curve in the bottom panel of Figure 7. Because $\rho_{p,\text{max}}$ does not vary significantly over the course of the spiral-in, the decrease in $\rho_{p,\text{max}}/\rho$ is driven almost entirely by the rise in ambient density. The descent of the densest planetary material halts where the ratio reaches 1, at $a = 0.12 R_\odot$. The material that has been ablated in the convective envelope will be mixed over many convective turnover times, which is ~ 100 days near the base of the convective zone. The deepest material, having penetrated into the radiative layer but having a larger mean molecular weight than its surroundings, is unstable against thermohaline convection, which may mix the material even deeper on the thermal time-scale (Vauclair 2004). Our simulation is incapable of capturing these processes as we do not model radiative and chemical diffusion.

5 DISCUSSION

5.1 Chemical enrichment signature

The amount of ablated planet mass in our simulations can be used to predict the surface chemical enrichment signature produced in the host star. Numerous studies have focused on the enrichment of Li, which is a sensitive measure of stellar evolution. Canonical stellar evolutionary models predict that Li is gradually depleted during red giant evolution, as the deepening of the convective region during the first dredge-up mixes Li-depleted material to the surface. Yet, $\approx 1.2\%$ of giant stars are Li-rich ($A(\text{Li}) > 1.5$) (e.g., Wallerstein & Sneden 1982; Balachandran et al. 2000; Drake et al. 2002; Ruchti et al. 2011; Monaco et al. 2011; Martell & Shetrone 2013; Casey et al. 2016; Kirby et al. 2016; Casey et al. 2019; Gao et al. 2019), prompting suggestions that planets, whose interiors are too cool to burn Li, could deposit Li-rich material into their hosts (Aguilera-Gómez et al. 2016; Soares-Furtado et al. 2021).

We estimate the surface Li enrichment signature from HJ engulfment, assuming the deposited planetary material has meteoritic Li abundance and becomes perfectly mixed inside the convective region. The absolute Li abundance observed at the stellar surface is then given by (Soares-Furtado et al. 2021)

$$A(\text{Li}) = 12 + \log_{10} \left(\frac{N_{\star,\text{cv}}(\text{Li}) + N_{p,\text{cv}}(\text{Li})}{N_{\star,\text{cv}}(\text{H}) + N_{p,\text{cv}}(\text{H})} \right), \quad (8)$$

where $N_{\star,\text{cv}}(\text{Li})$ and $N_{\star,\text{cv}}(\text{H})$ are the number of Li and H atoms initially present in the convective envelope, while $N_{p,\text{cv}}(\text{Li})$ and $N_{p,\text{cv}}(\text{H})$ are the number of Li and H atoms deposited by the planet into the convective envelope.

Our host star's convective envelope contains $M_{\text{cv}} = 0.75 M_\odot$ of material and we assume a H mass fraction of $X = 0.74$, yielding $N_{\star,\text{cv}}(\text{H}) = XM_{\text{cv}}/m_{\text{H}} = 6.6 \times 10^{56}$. We derive the baseline Li abundance from measurements of giant stars in the GALAH (GALactic Archaeology with HERMES) survey, using data compiled by Soares-Furtado et al. (2021) (associated with their Figure 1). The effective temperature and luminosity of our $1 M_\odot$ red giant model is consistent with a baseline abundance of $A(\text{Li}) \approx 0.85$. Given $N_{\star,\text{cv}}(\text{H})$, this implies $N_{\star,\text{cv}}(\text{Li}) = 4.7 \times 10^{45}$. We assume that the planet has the same H mass fraction as its host ($X = 0.74$) but with meteoritic Li abundance, $N(\text{Li})/N(\text{H}) = 2 \times 10^{-9}$ (Montalbán & Rebolo 2002). It follows

radiative zones to form beneath the layer where the heat is deposited. However, the mass contained in this radiative zone is insignificant

that it has $N_p(\text{H}) = (XM_p/m_{\text{H}}) = 8.8 \times 10^{53}$ H atoms and $N_p(\text{Li}) = (N(\text{Li})/N(\text{H}))N_p(\text{H}) = 1.8 \times 10^{45}$ Li atoms. In our simulations, ≈ 90 per cent of the total mass ($9 \times 10^{-4} M_{\odot}$) is deposited in the convective region, and so the number of H and Li atoms enriching the stellar surface are $N_{p,\text{cv}}(\text{H}) = 7.9 \times 10^{53}$ and $N_{p,\text{cv}}(\text{Li}) = 1.6 \times 10^{45}$, respectively. Inserting these values into equation (8) gives a surface absolute Li abundance of $A(\text{Li}) = 0.98$ after engulfment, or an enhancement of ≈ 0.13 dex.

This enhancement signature is not expected to be statistically significant, as it is comparable with the typical $A(\text{Li})$ spread in cluster red giants of ≈ 0.1 (Lind et al. 2009; Romano et al. 2021; Soares-Furtado et al. 2021). Soares-Furtado et al. (2021) estimate that the signature may persist for few $\times 10^7$ yr on the lower red giant branch, although they do not model uncertain processes like thermohaline mixing, elemental diffusion, and convective overshoot (see Théado & Vauclair 2012; Sevilla et al. 2022). HJ engulfment by a more expanded host star on the red giant branch would produce a stronger enrichment signature for the same amount of pollution, since (i) the baseline Li abundance decreases and (ii) the mass of the convective zone decreases due to the He core's growth and wind mass-loss. However, a more evolved giant also means the planet is engulfed with smaller velocities and interacts with a lower-density envelope. This reduces the amount of ablated material that could pollute the surface ($\dot{E}_{\text{hydro}} \sim R_{\star}^{-9/2}$, following from Section 2) unless tidal disruption still occurs in the convective envelope. Future studies can provide a more complete understanding by calculating the HJ mass ablation across host stars at different points in their evolution.

5.2 Induced stellar rotation

Planetary engulfment may impart significant rotation to the host star by transferring the planet's orbital angular momentum to the stellar envelope. This has been suggested to account for observations of rapidly-rotating giant stars (e.g., Soker & Harpaz 2000; Carlberg et al. 2013; Privitera et al. 2016b). We examine how planetary engulfment has impacted the azimuthal velocity profile, v_{ϕ} , as a function of cylindrical radius, R_{cylinder} , in Figure 9. The different coloured lines in the top panel show azimuthally-averaged $v_{\phi}(R_{\text{cylinder}})$ during the same snapshots shown in Figures 4 and 5. At $t = 0$, there is no rotation other than the orbital motion of the HJ itself, shown as the flat red segment at $4.0 < R_{\text{cylinder}}/R_{\odot} < 4.2$ with the local Keplerian velocity, 216 km s^{-1} . The grazing interaction causes a low-density surface layer to expand beyond the initial stellar radius of $4 R_{\odot}$. This material spins up to 100 km s^{-1} , although representing a very small amount of mass. This is illustrated by the bottom panel of Figure 9, which plots the mass exterior to a given value of R_{cylinder} . By the end of the simulation (dark blue curve), only the outermost $\sim 10^{-3} M_{\odot}$ of material rotates faster than 10 km s^{-1} . The bulk of the stellar envelope is slowly rotating ($v_{\phi} \sim 1 \text{ km s}^{-1}$), in agreement with the simulations by Staff et al. (2016) for red giant and asymptotic giant branch stars. Furthermore, this angular momentum will be redistributed on a much longer time-scale than simulated. Modelling this process is beyond the scope and capabilities of simple adiabatic simulations, which neglect, e.g., convection and magnetic fields. But it is straightforward to estimate the maximum spin-up by assuming angular momentum conservation as follows.

The induced velocities are slightly faster than the envelope's convective eddies. That is, the envelope has a small convective Rossby number ($Ro \lesssim 1$), which is defined as the ratio of the rota-

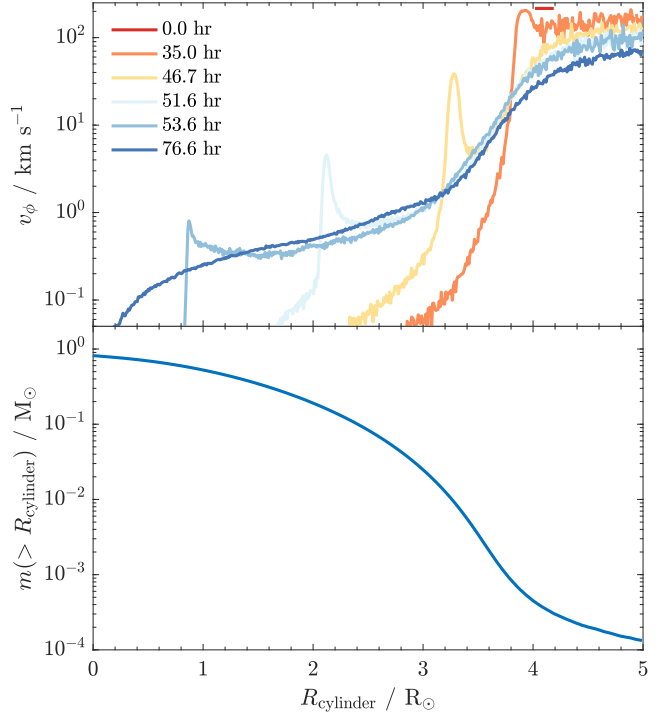


Figure 9. *Top panel:* The azimuthal velocity, v_{ϕ} , as a function of cylindrical radius, R_{cylinder} , at different points in time corresponding to the snapshots in Figure 4. *Bottom panel:* The mass exterior to R_{cylinder} . At $t = 0$, there is no rotation other than the orbital motion of the hot Jupiter itself, which is shown as a flat red line at the Keplerian velocity, 216 km s^{-1} . The inward movement of the hot Jupiter is shown by the spike. In the last simulation snapshot, the outermost $\approx 10^{-3} M_{\odot}$ of material rotates at few $\times 10 \text{ km s}^{-1}$.

tional period to the convective turnover time-scale. In this case, it is the ratio of the Brunt-Väisälä frequency to the imparted angular frequency. In the small Ro regime, angular momentum is redistributed to produce rigid rotation. Assuming the orbital angular momentum is perfectly transferred into the convective envelope's rotation,

$$I_{\text{env}} \Omega_{\text{env}} = M_p R_{\star}^2 \Omega_{\text{orb}}. \quad (9)$$

I_{env} is the convective region's moment of inertia, assumed to be unaltered by the engulfment process as appropriate for the small mass ratio at hand. Engulfing more massive planets or brown dwarfs is likely to inflate a more evolved host star, significantly increasing its moment of inertia before contracting on the thermal time-scale. Ω_{env} is the angular velocity the envelope rotates with as a rigid body after engulfment. The right-hand side is the planet's orbital angular momentum upon entering the host star on a circular orbit, with angular velocity $\Omega_{\text{orb}} = (GM_{\star}/R_{\star}^3)^{1/2}$. The increase in surface rotational velocity, $\Delta v_{\text{rot}} = \Omega_{\text{env}} R_{\star}$, can then be solved, giving

$$\Delta v_{\text{rot}} \approx 1.7 \text{ km s}^{-1} \left(\frac{k_{\text{env}}}{0.13} \right)^{-1} \left(\frac{M_p/M_{\star}}{10^{-3}} \right) \left(\frac{M_{\star}}{1 M_{\odot}} \right)^{1/2} \left(\frac{R_{\star}}{4 R_{\odot}} \right)^{-1/2}, \quad (10)$$

where we have expressed the convective envelope's moment of inertia in terms of an apsidal motion constant k_{env} , defined via $I_{\text{env}} = k_{\text{env}} M_{\star} R_{\star}^2$. k_{env} is generally a quantity of the order of 0.1 for evolved giant stars, and decreases with age as the star becomes more centrally concentrated. For our stellar model, $k_{\text{env}} = 0.13$, which yields $\Delta v_{\text{rot}} = 1.7 \text{ km s}^{-1}$ according to equation (10).

Our estimate is roughly consistent with the velocity magnitudes observed in the bulk of the envelope ($R_{\text{cylinder}} \lesssim 3.5 R_{\odot}$)

in the last profile shown in Figure 9. The linear scaling of Δv_{rot} with M_p implies that engulfing a 10 M_J companion could produce envelope rotation velocities up to 17 km s^{-1} . Recently, the red giant KIC 9267654 was reported to have a surface that rotates more rapidly than the bulk of its envelope (Tayar et al. 2022), which led to the suggestion that it had recently ingested a planet. Our simulation suggests that planetary engulfment could account for this non-monotonic rotation profile, although the duration of this state depends on the uncertain efficiencies of angular momentum transport mechanisms. This could be studied by mapping the rotation profile obtained at the end of our simulation into a detailed stellar evolution code like MESA.

5.3 Luminous transients

Planetary engulfment can produce a luminous transient powered by orbital decay, where orbital energy is deposited into the host star via drag. Observable transients are expected for engulfments occurring on the subgiant and on the lower red giant branch (MacLeod et al. 2018), since smaller stellar radii imply larger orbital velocities and envelope densities at contact ($\dot{E}_{\text{hydro}} \propto \rho v^3$). Moreover, because the injected luminosity has to compete with the background stellar luminosity, it is more likely to be detectable in less evolved and therefore less luminous stars.

During the early parts of the grazing phase, energy is deposited in surface layers where it may be quickly transported to the photosphere and be radiated away before being able to thermalise. Therefore, the observed luminosity directly tracks the drag luminosity (given it is larger than the unperturbed stellar luminosity), slowly increasing with the planet's depth due to encountering denser and higher-velocity gas. Our simulation does not capture the photometric transient during this phase, as it requires resolving the low-density photosphere and modelling radiation transport. At the chosen resolution, the initial stellar surface is resolved down to $10^{-4} \text{ g cm}^{-3}$, which is three orders of magnitude denser than the photosphere (see Section 4.1). The photon diffusion time from this layer to the surface is several decades and the adiabatic assumption is well justified. The transient from the early grazing phase can be modelled using one dimensional calculations that self-consistently include drag heating from the engulfed planet and model energy transport in these layers (Cantiello et al. in prep.).

During the later parts of grazing and the transition to full engulfment, the energy injection rate continues to increase with planet depth. At the same time, the energy transport time-scale grows and exceeds the orbital decay time-scale, and so the injected orbital energy is thermalised in the envelope and increases the stellar luminosity once it is transported to the photosphere. So the qualitative expectation for the transient is a slow luminosity increase during the grazing phase, followed by a relatively sharp peak in luminosity during the early part of the engulfment phase, followed by a slow decrease of stellar luminosity to pre-engulfment values on the envelope's thermal time-scale. Indeed the secular dimming induced by a planetary engulfment might have been observed in KIC 8462852 (Metzger et al. 2017). Yarza et al. (2022) predict that HJs engulfed on the red giant branch at $10 R_{\odot}$ separations could brighten the star by factors of several hundreds for about 1 yr, but up to 5,000 yr if engulfing a 50 M_J brown dwarf.

Another source of photometric variability can be provided by the expansion, cooling, and recombination of material ejected from the engulfment process. In our model, about $1.6 \times 10^{-5} M_{\odot}$ of material becomes unbound. This is an upper limit as all injected

energy is used to expand the stellar gas in our adiabatic simulations, as opposed to being radiated away. While radiative diffusion is inefficient, the convective turnover time near the surface may compete with the energy injection time-scale, and therefore convection may prevent some fraction of the drag luminosity from driving surface expansion. Within the adiabatic assumption, the order of magnitude of the unbound mass is a fairly robust result, although the exact amount has not converged with resolution (see Appendix A). Applying the scaling relation of Matsumoto & Metzger (2022) for the H-recombination luminosity of unbound material and assuming that $10^{-5} M_{\odot}$ of material escapes with 300 km s^{-1} (roughly the surface escape velocity) gives a peak luminosity of about $2 \times 10^{35} \text{ erg s}^{-1}$, which is almost ten times the unperturbed stellar luminosity, and a plateau duration of about 3 days. The estimate of Matsumoto & Metzger (2022) may break down if the ejecta is significantly radiation pressure dominated or deviates from spherical geometry, which could be studied in the future.

It is then possible that some planetary engulfments might exhibit lightcurves with two peaks: the first associated with drag-heating of the near-surface stellar layers, and the second due to H-recombination in ejected material. Their relative importance is dependent on the host star's evolutionary phase. For planetary engulfment occurring further up the red giant branch, the surface drag luminosity cannot surpass the background stellar luminosity (MacLeod et al. 2018), and so H-recombination may be the only source of photometric variability. At the same time, these evolved red giants have more loosely bound envelopes, and so may produce more unbound ejecta in an engulfment episode.

6 SUMMARY AND CONCLUSIONS

We performed a 3D hydrodynamical simulation of HJ engulfment by a $1 M_{\odot}$ star located on the lower part of the red giant branch, where it has expanded to a radius of $4 R_{\odot}$. This scenario has been chosen to reflect star-planet interaction at the smallest separation that would still confidently lead to a direct merger, i.e., averting planet Roche-lobe overflow or tidal disruption outside the star. It could represent the fate of observed ultra-short period HJs, or longer-period Jovian planets that migrate inwards due to tides. In the simulated regime, drag from ram pressure rather than gravitational focussing of upstream gas drives the spiral-in. To self-consistently model ram pressure, and also to capture other effects like mass ablation and disruption, we modelled the HJ as a polytropic gas sphere.

We identify four different phases of engulfment, similar to those outlined by Metzger et al. (2012) and Jia & Spruit (2018). An initial grazing phase is characterised by relatively slow spiral-in near the stellar surface, where the density scale height ranges from a few $\times 0.1 - 1 R_J$. The main engulfment phase proceeds when the HJ becomes completely immersed within the stellar envelope, and spirals towards the core in roughly a single orbit. The strong drag force gives rise to a sinking stage where radial in-fall dominates azimuthal motion, ending in disruption by a combination of tides and ram pressure from the dense radiative layers beneath the outer convective zone. The disrupted planetary fragments sink until reaching density equilibrium with their surroundings.

The HJ gradually dissipates ≈ 90 per cent of its mass into the convective region, which may enrich the stellar surface with Li and heavy elements after mixing. Our resolution test suggests that the total amount of mass loss is robust, although the precise amount that is ablated at different separations has not fully converged. Further work should quantify the effects of any resolution-dependent

heating that might have artificially enhanced ablation, particularly during the grazing stage. We estimate that Li is enhanced by 0.13 dex, which is not statistically significant given the intrinsic A(Li) variation in open clusters has a similar magnitude. Producing a stronger enrichment signature would require engulfing or accreting more massive substellar bodies (e.g. brown dwarfs) onto stars that have evolved further along the red giant branch, where the baseline Li abundance and convective mass decrease.

Significant ($\gtrsim 10 \text{ km s}^{-1}$) surface rotational velocities are observed at the end of our simulation, although representing a very small amount of mass ($\sim 10^{-3} M_{\odot}$). The bulk of the envelope rotates with $\sim 1 \text{ km s}^{-1}$, consistent with the analytical expectation from angular momentum conservation. The maximum induced surface rotational speed scales linearly with the mass of the engulfed object, and so could reach $\sim 10 \text{ km s}^{-1}$ from engulfing a more compact, say $10 M_J$, HJ.

The orbital energy deposited via drag into the stellar envelope may produce a luminous transient, particularly for engulfment events occurring on the subgiant or lower part of the red giant branch. The small amount of unbound ejecta, $\sim 10^{-5} M_{\odot}$ in our simulation, could give rise to a second, recombination-powered peak in the lightcurve that is ten times more luminous than the unperturbed star.

Our work focused on a specific choice of host star and planet. Future work could apply this approach to study the chemical enrichment signature and induced stellar rotation across a wide parameter region. Where the host star is significantly altered by planetary engulfment, its long-term evolution can also be studied by mapping the structure obtained at the end of 3D simulations to 1D stellar evolution codes.

ACKNOWLEDGEMENTS

This work has benefited from useful discussions with Tatsuya Matsumoto, Brian Metzger, Ryosuke Hirai, Andy Casey, and Amanda Karakas. We further thank Melinda Soares-Furtado for sharing the GALAH A(Li) data (Soares-Furtado et al. 2021) used in our estimate of the Li enrichment signature. This paper made use of data from the NASA Exoplanet Archive, which is operated by the California Institute of Technology, under contract with the National Aeronautics and Space Administration under the Exoplanet Exploration Program. The simulations presented in this work were performed on the Rusty supercomputer and Popeye supercomputer of the Flatiron Institute, which is supported by Simons Foundation. M. Y. M. L. acknowledges support by an Australian Government Research Training Program (RTP) Scholarship. I.M. is a recipient of the Australian Research Council Future Fellowship FT190100574. Parts of this research were supported by the Australian Research Council Centre of Excellence for Gravitational Wave Discovery (OzGrav), through project number CE170100004.

DATA AVAILABILITY

The MESA stellar model used in our simulations, the in-list used to generate the model, and data that were used to produce all figures in this article are available at <https://dx.doi.org/10.26180/21342090>.

REFERENCES

- Abia C., Cabezón R. M., Domínguez I., 2020, *Mem. Soc. Astron. Italiana*, **91**, 48
- Adamów M., Niedzielski A., Kowalik K., Villaver E., Wolszczan A., Maciejewski G., Gromadzki M., 2018, *A&A*, **613**, A47
- Aguilera-Gómez C., Chanamé J., Pinsonneault M. H., Carlberg J. K., 2016, *ApJ*, **829**, 127
- Akeson R. L. et al., 2013, *PASP*, **125**, 989
- Alexander J. B., 1967, *The Observatory*, **87**, 238
- Balachandran S. C., Fekel F. C., Henry G. W., Uitenbroek H., 2000, *ApJ*, **542**, 978
- Barker A. J., 2020, *MNRAS*, **498**, 2270
- Bayliss D. D. R., Sackett P. D., 2011, *ApJ*, **743**, 103
- Bondi H., 1952, *MNRAS*, **112**, 195
- Cameron A. G. W., Fowler W. A., 1971, *ApJ*, **164**, 111
- Carlberg J. K., Majewski S. R., Patterson R. J., Bizyaev D., Smith V. V., Cunha K., 2011, *ApJ*, **732**, 39
- Carlberg J. K., Cunha K., Smith V. V., Majewski S. R., 2013, *Astronomische Nachrichten*, **334**, 120
- Carlos M., Nissen P. E., Meléndez J., 2016, *A&A*, **587**, A100
- Casey A. R. et al., 2016, *MNRAS*, **461**, 3336
- Casey A. R. et al., 2019, *ApJ*, **880**, 125
- Chandrasekhar S., 1943, *ApJ*, **97**, 255
- Chow E., Monaghan J. J., 1997, *Journal of Computational Physics*, **134**, 296
- Cullen L., Dehnen W., 2010, *MNRAS*, **408**, 669
- Cumming A., Butler R. P., Marcy G. W., Vogt S. S., Wright J. T., Fischer D. A., 2008, *PASP*, **120**, 531
- Dawson R. I., Johnson J. A., 2018, *ARA&A*, **56**, 175
- De S., MacLeod M., Everson R. W., Antoni A., Mandel I., Ramirez-Ruiz E., 2020, *ApJ*, **897**, 130
- Dobbs-Dixon I., Lin D. N. C., Mardling R. A., 2004, *ApJ*, **610**, 464
- Drake N. A., de la Reza R., da Silva L., Lambert D. L., 2002, *AJ*, **123**, 2703
- Eggleton P. P., 1983, *ApJ*, **268**, 368
- Eggleton P. P., Kiseleva-Eggleton L., 2001, *ApJ*, **562**, 1012
- Faber J. A., Rasio F. A., Willems B., 2005, *Icarus*, **175**, 248
- Fabrycky D., Tremaine S., 2007, *ApJ*, **669**, 1298
- Fortney J. J., Dawson R. I., Komacek T. D., 2021, *Journal of Geophysical Research (Planets)*, **126**, e06629
- Fossati L. et al., 2010, *ApJ*, **714**, L222
- Fressin F. et al., 2013, *ApJ*, **766**, 81
- Gao Q., Shi J.-R., Yan H.-L., Yan T.-S., Xiang M.-S., Zhou Y.-T., Li C.-Q., Zhao G., 2019, *ApJS*, **245**, 33
- Ginzburg S., Sari R., 2017, *MNRAS*, **469**, 278
- Gonzalez-Bolivar M., De Marco O., Lau M. Y. M., Hirai R., Price D. J., 2022, *MNRAS*, **pp 3181–3199**
- Gould A., Dorsher S., Gaudi B. S., Udalski A., 2006, *Acta Astron.*, **56**, 1
- Guillochon J., Ramirez-Ruiz E., Lin D., 2011, *ApJ*, **732**, 74
- Guillot T., Stevenson D. J., Hubbard W. B., Saumon D., 2004, in Bagenal F., Dowling T. E., McKinnon W. B., eds., *Vol. 1, Jupiter. The Planet, Satellites and Magnetosphere*. Cambridge University Press, pp 35–57
- Gurevich O., Bear E., Soker N., 2022, *MNRAS*, **511**, 1330
- Hebb L. et al., 2009, *ApJ*, **693**, 1920
- Hellier C. et al., 2009, *Nature*, **460**, 1098
- Hirai R., Sawai H., Yamada S., 2014, *ApJ*, **792**, 66
- Hirai R., Sato T., Podsiadlowski P., Vigna-Gómez A., Mandel I., 2020, *MNRAS*, **499**, 1154
- Howard A. W. et al., 2012, *ApJS*, **201**, 15
- Hoyle F., Lyttleton R. A., 1939, *Proceedings of the Cambridge Philosophical Society*, **35**, 405
- Hubbard W. B., 1984, *Planetary interiors*. Van Nostrand Reinhold
- Israelian G., 2002, *Journal of Astronomical Data*, **8**, 8
- Ivanova N., Podsiadlowski P., Spruit H., 2002, *MNRAS*, **334**, 819
- Jackson B., Barnes R., Greenberg R., 2009, *ApJ*, **698**, 1357
- Jackson B., Jensen E., Peacock S., Arras P., Penev K., 2016, *Celestial Mechanics and Dynamical Astronomy*, **126**, 227
- Jia S., Spruit H. C., 2017, *MNRAS*, **465**, 149
- Jia S., Spruit H. C., 2018, *ApJ*, **864**, 169

Jurić M., Tremaine S., 2008, *ApJ*, **686**, 603
 Kirby E. N., Guhathakurta P., Zhang A. J., Hong J., Guo M., Guo R., Cohen J. G., Cunha K., 2016, *ApJ*, **819**, 135
 Komacek T. D., Thorngren D. P., Lopez E. D., Ginzburg S., 2020, *ApJ*, **893**, 36
 Kunitomo M., Ikoma M., Sato B., Katsuta Y., Ida S., 2011, *ApJ*, **737**, 66
 Lau M. Y. M., Hirai R., González-Bolívar M., Price D. J., De Marco O., Mandel I., 2022a, *MNRAS*, **512**, 5462
 Lau M. Y. M., Hirai R., Price D. J., Mandel I., 2022b, *MNRAS*
 Lazovik Y. A., 2021, *MNRAS*, **508**, 3408
 Li S.-L., Miller N., Lin D. N. C., Fortney J. J., 2010, *Nature*, **463**, 1054
 Lind K., Primas F., Charbonnel C., Grundahl F., Asplund M., 2009, *A&A*, **503**, 545
 Liu S.-F., Guillochon J., Lin D. N. C., Ramirez-Ruiz E., 2013, *ApJ*, **762**, 37
 Livio M., Soker N., 1984, *MNRAS*, **208**, 763
 Lopez E. D., Fortney J. J., 2016, *ApJ*, **818**, 4
 MacLeod M., Ramirez-Ruiz E., 2015, *ApJ*, **803**, 41
 MacLeod M., Antoni A., Murguía-Berthier A., Macías P., Ramirez-Ruiz E., 2017, *ApJ*, **838**, 56
 MacLeod M., Cantiello M., Soares-Furtado M., 2018, *ApJ*, **853**, L1
 Marcy G., Butler R. P., Fischer D., Vogt S., Wright J. T., Tinney C. G., Jones H. R. A., 2005, *Progress of Theoretical Physics Supplement*, **158**, 24
 Mardling R. A., 1995, *ApJ*, **450**, 722
 Martell S. L., Shetrone M. D., 2013, *MNRAS*, **430**, 611
 Matsumoto T., Metzger B. D., 2022, preprint ([arXiv:2202.10478](https://arxiv.org/abs/2202.10478))
 Mayor M., Queloz D., 1995, *Nature*, **378**, 355
 Mayor M. et al., 2011, preprint ([arXiv:1109.2497](https://arxiv.org/abs/1109.2497))
 Meléndez J., Schirbel L., Monroe T. R., Yong D., Ramírez I., Asplund M., 2014, *A&A*, **567**, L3
 Metzger B. D., Giannios D., Spiegel D. S., 2012, *MNRAS*, **425**, 2778
 Metzger B. D., Shen K. J., Stone N., 2017, *MNRAS*, **468**, 4399
 Miller N., Fortney J. J., Jackson B., 2009, *ApJ*, **702**, 1413
 Monaco L. et al., 2011, *A&A*, **529**, A90
 Monaghan J. J., 1992, *ARA&A*, **30**, 543
 Monroe T. R. et al., 2013, *ApJ*, **774**, L32
 Montalbán J., Rebolo R., 2002, *A&A*, **386**, 1039
 Nagar T., Spina L., Karakas A. I., 2019, preprint ([arXiv:1911.09861](https://arxiv.org/abs/1911.09861))
 Nagasawa M., Ida S., Bessho T., 2008, *ApJ*, **678**, 498
 Naoz S., Farr W. M., Lithwick Y., Rasio F. A., Teyssandier J., 2011, *Nature*, **473**, 187
 Naoz S., Farr W. M., Rasio F. A., 2012, *ApJ*, **754**, L36
 Ostriker E. C., 1999, *ApJ*, **513**, 252
 Paxton B., Bildsten L., Dotter A., Herwig F., Lesaffre P., Timmes F., 2011, *ApJS*, **192**, 3
 Paxton B. et al., 2013, *ApJS*, **208**, 4
 Paxton B. et al., 2015, *ApJS*, **220**, 15
 Paxton B. et al., 2018, *ApJS*, **234**, 34
 Paxton B. et al., 2019, *ApJS*, **243**, 10
 Price D. J., 2007, *Publ. Astron. Soc. Australia*, **24**, 159
 Price D. J., 2008, *Journal of Computational Physics*, **227**, 10040
 Price D. J., 2012, *Journal of Computational Physics*, **231**, 759
 Price D. J. et al., 2018, *Publications of the Astronomical Society of Australia*, **35**, e031
 Privitera G., Meynet G., Eggenberger P., Vidotto A. A., Villaver E., Bianda M., 2016a, *A&A*, **591**, A45
 Privitera G., Meynet G., Eggenberger P., Vidotto A. A., Villaver E., Bianda M., 2016b, *A&A*, **593**, A128
 Rasio F. A., Ford E. B., 1996, *Science*, **274**, 954
 Rasio F. A., Tout C. A., Lubow S. H., Livio M., 1996, *ApJ*, **470**, 1187
 Romano D. et al., 2021, *A&A*, **653**, A72
 Ruchti G. R. et al., 2011, *ApJ*, **743**, 107
 Sandquist E., Taam R. E., Lin D. N. C., Burkert A., 1998, *ApJ*, **506**, L65
 Sandquist E. L., Dokter J. J., Lin D. N. C., Mardling R. A., 2002, *ApJ*, **572**, 1012
 Sevilla J., Behrard A., Fuller J., 2022, *MNRAS*, **516**, 3354
 Siess L., Livio M., 1999, *MNRAS*, **304**, 925
 Soares-Furtado M., Cantiello M., MacLeod M., Ness M. K., 2021, *AJ*, **162**, 273

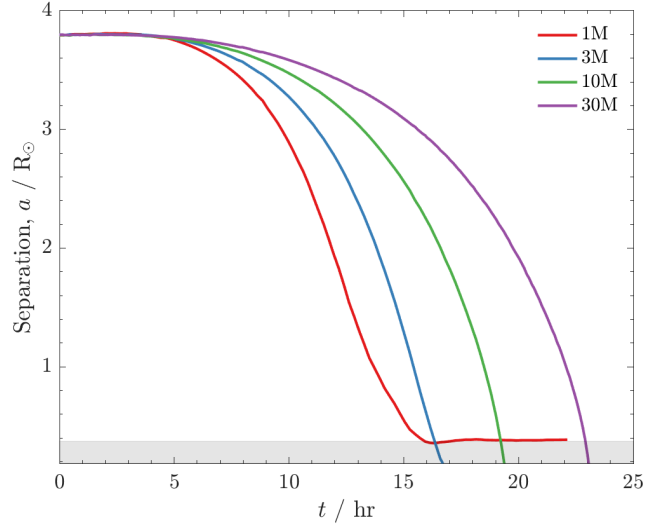


Figure A1. Comparison of the evolution in planet separation, a , at different resolutions as indicated by the total number of SPH particles used to resolve the star (N_*) in each simulation. The shaded region is beneath the star's core excision radius.

Soker N., Harpaz A., 2000, *MNRAS*, **317**, 861
 Soker N., Livio M., Harpaz A., 1984, *MNRAS*, **210**, 189
 Southworth J. et al., 2015, *MNRAS*, **447**, 711
 Staff J. E., De Marco O., Wood P., Galaviz P., Passy J.-C., 2016, *MNRAS*, **458**, 832
 Stephan A. P., Naoz S., Gaudi B. S., 2018, *AJ*, **156**, 128
 Stephan A. P., Naoz S., Gaudi B. S., Salas J. M., 2020, *ApJ*, **889**, 45
 Stevenson D. J., 1991, *ARA&A*, **29**, 163
 Tayar J. et al., 2022, preprint ([arXiv:2208.01678](https://arxiv.org/abs/2208.01678))
 Théado S., Vauclair S., 2012, *ApJ*, **744**, 123
 Valsecchi F., Rasio F. A., Steffen J. H., 2014, *ApJ*, **793**, L3
 Valsecchi F., Rappaport S., Rasio F. A., Marchant P., Rogers L. A., 2015, *ApJ*, **813**, 101
 Vauclair S., 2004, *ApJ*, **605**, 874
 Villaver E., Livio M., 2007, *ApJ*, **661**, 1192
 Villaver E., Livio M., 2009, *ApJ*, **705**, L81
 Wallerstein G., Sneden C., 1982, *ApJ*, **255**, 577
 Weidenschilling S. J., Marzari F., 1996, *Nature*, **384**, 619
 Wong I., Shporer A., Vissapragada S., Greklek-McKeon M., Knutson H. A., Winn J. N., Benneke B., 2022, *AJ*, **163**, 175
 Wright J. T., Marcy G. W., Howard A. W., Johnson J. A., Morton T. D., Fischer D. A., 2012, *ApJ*, **753**, 160
 Wu Y., Murray N., 2003, *ApJ*, **589**, 605
 Wu Y., Murray N. W., Ramsahai J. M., 2007, *ApJ*, **670**, 820
 Yorza R. et al., 2022, preprint ([arXiv:2203.11227](https://arxiv.org/abs/2203.11227))

APPENDIX A: RESOLUTION STUDY

To study the resolution dependence of our results, we produce a grid of four different simulations that resolve the star with $N_* = 10^6$, 3×10^6 , 10^7 , and 3×10^7 SPH particles. Due to the use of equal-mass particles in PHANTOM, the number of particles that is initially used to resolve the planet in each case is $M_p N_*/(M_* - M_{\text{core}}) = 1262, 3786, 12616$, and 37846 , respectively. Because we are most interested in whether the evolution of M_p and a have converged, we focus on simulating the engulfment phase, where these quantities change the most. We therefore start with the HJ being fully immersed in the stellar envelope ($a(t=0) = 3.8 R_\odot$) and also use a larger core boundary than in our main simulation, $r_{\text{core}} = 0.372 R_\odot$ and

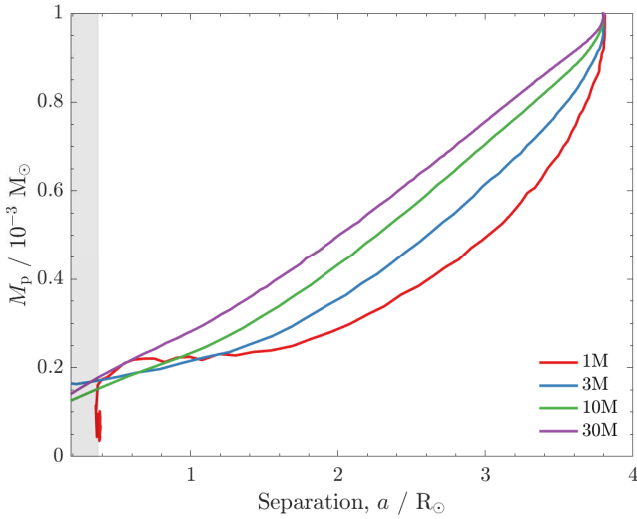


Figure A2. Comparison of the evolution in planet mass, M_p , as a function of separation, a , at different resolutions as indicated by the total number of SPH particles used to resolve the star (N_\star) in each simulation. The shaded region is beneath the star's core excision radius.

$M_{\text{core}} = 0.207 M_\odot$. Both measures reduce the dynamic range such that the higher-resolution simulation (with $N_\star = 3 \times 10^7$) is feasible.

Figure A1 shows the time evolution of a at different resolutions. The simulations have yet to converge on the duration of the engulfment phase, with higher resolution resulting in a longer spiral-in. The cause of this has been raised in Section 4.1: higher resolution better resolves the low-density stellar surface. When setting up the 3D star, under-resolving the pressure scale height at the surface causes slight expansion during the relaxation phase, resulting in a higher density compared to the MESA model at the same radius. This increases the drag luminosity near the surface, and shortens the length of the grazing phase and transition to full engulfment. We have also restricted Figure A1 to $a > r_{\text{core}}/2$, as the in-spiral beneath the inner boundary has no physical meaning, and the stellar density near r_{core} for our resolution study is generally too low for the disrupted planetary material to settle. The $N_\star = 10^6$ simulation (red curve) is an exception, where the densest material stalls at $a \approx 0.37 R_\odot$ because the HJ's central density decreases sufficiently over the engulfment process for it to become neutrally buoyant at that radius.

Figure A2 shows the resolution dependence of HJ ablation. As discussed in Section 4.3, the initial mass loss, concentrated at $a = 3.8 R_\odot$, is overestimated at low resolution. This could be because the SPH conductivity that is active when resolving steep density gradients in low-density regions artificially heats the HJ. But the ablation rate in the later parts of engulfment decreases to give nearly the same overall mass that is lost to the convective envelope across different resolutions. The SPH conductivity, which is second order in the particle smoothing length, decreases towards the denser stellar interior. With the $N_\star = 10^7$ and 3×10^7 simulations (green and purple curves), the apparent mass loss at the onset of engulfment is no longer present, and M_p instead decreases linearly with a . The final HJ mass, near $a = r_{\text{core}}$, appears robust as it falls within the range of $1.5\text{--}2.0 \times 10^{-3} M_\odot$ across all tested resolutions.

The amount of unbound mass, which is relevant for understanding the recombination transient discussed in Section 5.3, changes by a factor of a few across the different simulations. For $N_\star = 10^6$, 3×10^6 , 10^7 , and 3×10^7 , the amount of unbound material are 2.0,

1.6, 1.1, and 0.82, respectively, in units of $10^{-5} M_\odot$. The amount of unbound ejecta therefore decreases with resolution, likely to be also related to the ability to resolve the low-density stellar surface, where much of the unbound material originates. However, increasing the starting orbital separation, which lengthens the grazing phase, also leads to a larger amount of unbound mass. The default simulation, carried out with $N_\star = 10^7$ and starting at $a(t=0) = 4.1 R_\odot$, ejects $1.6 \times 10^{-5} M_\odot$ of material, compared to the $1.1 \times 10^{-5} M_\odot$ of material ejected in the resolution test with the same N_\star but starting at $a(t=0) = 3.8 R_\odot$. The amount of unbound ejecta is therefore a considerable source of uncertainty in our estimate of the plateau luminosity and duration of the H-recombination transient in Section 5.3.

Overall, the resolution study shows that our simulation likely underestimates the length of the grazing phase and delays the onset of the engulfment stage. However, the conclusion that the planet loses ≈ 90 per cent of its mass in the convective envelope is robust, and the mass ablation rate appears to be a constant function of separation. The amount of unbound ejecta decreases with resolution but increases with the initial planet separation, though all lying within the order of $10^{-5} M_\odot$ across the tested resolutions.

This paper has been typeset from a \LaTeX file prepared by the author.